A New Aneurysm Rupture-Prone Marfan Mouse Model with FBN1Q2467X Nonsense Mutation Reveals Adventitial Inflammation

Shichao Wu[1,7#], Jiawei Zhao[1#], Alejandro Ponce[1#], Lucynda Pham[1,2], Daniel Xie[1], Donghong Ju[1,4], Francis Hernandez[1], Sean Jones[1], Clair Li[1], Charles S. Chung[5], Dragana Komnenov[1], Noreen F. Rossi[5], Zhe Yang[7], Maozhou Yang[8], Hui Li[9], Youming Xie[3,4], Kang Chen [2,4,6,7], Kezhong Zhang[2,7] and Li Li[1,2,3*]

[1]Department of Internal Medicine, [2]Center for Molecular Medicine and Genetics, [3]Ann Karmanos Cancer Institute, [4]Department of Oncology, [5]Department of Physiology, [6]Department of Obstetrics and Gynecology, [7]Department of Biochemistry Microbiology and Immunology, [8]Bone and Joint Center, Henry Ford Hospital, Detroit, MI 48202; [9]Department of Medicine, University of Massachusetts, Worcester, MA, 01655.

Running Title: **An Aneurysm Rupture-Prone Marfan Mouse Model with *FBN1Q2467X***

# These authors contributed equally to this work.

* Correspondence and requests for materials should be addressed to L.L. (lili@med.wayne.edu).

Li Li, Ph.D.

Department of Internal Medicine

Center for Molecular Medicine & Genetics

Cardiovascular Research Institute

Wayne State University

421 E. Canfield Ave. #2146

Detroit MI 48201

(313) 577-8749 (office)

lili@med.wayne.edu

Word count: 9656 Total number of Figures: 8

Abstract: Marfan syndrome (MFS) is a genetic disorder caused by mutations in *FBN1*, which encodes fibrillin-1, a critical component of the extracellular matrix. Mutations in *FBN1* influence both the severity of aortic disease and responses to therapy, with aortic aneurysm being the leading cause of mortality in MFS patients. We generated a Marfan mouse model ($Fbn1^{Q2469X/+}$) carrying the FBN1Q2467X nonsense mutation identified in patients. This mutation results in fibrillin-1 deficiency and predisposes heterozygous mice to aortic root dilation and ascending aortic aneurysm under metabolic stress, such as a high-fat diet. Homozygous $Fbn1^{Q2469X/Q2469X}$ mice develop spontaneous thoracic aortic aneurysms that uniformly progress to rupture between 10 and 25 days of age, with 100% penetrance. Histopathology shows progressive vessel wall degeneration characterized by disorganized vascular smooth muscle cells, collagen loss, and elastic fiber fragmentation from early to late stages. Transcriptomic analysis identifies inflammation as the dominant process in late-stage aneurysms. Immunofluorescence assay reveals inflammatory cells prominently localized to the adventitia near rupture sites, linking adventitial inflammation to aneurysm progression. This genetically engineered Marfan model consistently develops rupture-prone aneurysms and provides a reliable, cost-effective platform for dissecting molecular mechanisms of aneurysm progression and for evaluating therapeutic strategies in Marfan syndrome and related aneurysm disorders.

Introduction:

Marfan syndrome (MFS) is a heritable connective tissue disorder that affects the cardiovascular, skeletal, ocular, and pulmonary systems [1-5]. Aortic aneurysm and dissection are the leading causes of mortality in MFS patients, underscoring the urgent need for improved understanding of disease mechanisms and therapeutic strategies. MFS is primarily caused by mutations in *FBN1*, which encodes fibrillin-1 (FBN1), an essential extracellular matrix protein that provides structural support and regulates inter and intracellular signaling [2,6]. More than 3,000 pathogenic variants in *FBN1* have been identified, including missense, nonsense, and frameshift mutations, each with distinct consequences for protein function and abundance [4,7]. Clinical studies demonstrate that aneurysm severity varies depending on mutation type [8,9]:, suggesting that different classes of mutations activate overlapping but not identical pathogenic pathways. Patients with haploinsufficiency mutations, such as nonsense or frameshift variants, generally develop more aggressive aortic disease than those with many dominant-negative missense mutations, except for variants in exons 24–32 associated with infantile MFS[9,10]. Understanding why haploinsufficiency leads to more severe phenotypes remains a critical unanswered question.

Therapeutic response in MFS also appears to be mutation specific. Angiotensin II receptor blockade with losartan has been shown to attenuate aortic root dilation in patients carrying nonsense and frameshift mutations, but its benefit is less pronounced in those with missense variants [11-14]. These findings suggest that molecular context, haploinsufficiency versus dominant-negative mutation, determines not only disease severity but also treatment efficacy. The development of mutation-relevant animal models is therefore essential for understanding the underlying mechanisms of aortic disease and for guiding precision therapies in MFS.

Current widely used Marfan mouse models have provided important insights into aneurysm pathogenesis but have key limitations. The *Fbn1*^{C1041G} model, which carries a patient-derived missense mutation [15], while the *Fbn1*$^{mgR/mgR}$ (MgR) model, generated by an aberrant recombination event that reduces *Fbn1* expression, has been used as a hypomorphic system [16]. However, neither model reflects haploinsufficiency caused by nonsense mutations. Moreover, existing models often show variable timing and incomplete penetrance of aneurysm rupture, complicating efforts to study late-stage disease. Thus, there remains a pressing need for a reliable, rupture-prone mouse model that incorporates a clinically relevant nonsense mutation.

To address this gap, we used the CRISPR/Cas9 genome editing technology to generate a new Marfan mouse model *Fbn1*$^{Q2469X/+}$, harboring the FBN1Q2467X nonsense mutation found in Marfan patients)[17,18]. Heterozygous mice develop aortic root dilation and ascending aneurysms under metabolic stress, while homozygous mice uniformly develop thoracic aortic aneurysms that rupture within 10–25 days of age. Histopathological and transcriptomic analyses reveal smooth muscle cell remodeling, extracellular matrix degradation, and oxidative stress, with inflammatory cells prominently localized in the adventitia near rupture sites. These findings identify adventitial inflammation as a hallmark of late-stage disease. This rupture-prone model provides a consistent and cost-effective platform to investigate the molecular mechanisms underlying aneurysm progression and to evaluate therapeutic strategies for MFS and related aneurysm disorders.

Material and Methods:

Generation of *Fbn1*$^{Q2469X/+}$ Mice The FBN1 gene is highly conserved between humans and mice: the human nonsense mutation *FBN1* c.7399C>T (p.Q2467X) in exon 59 corresponds to mouse *Fbn1* c.7405C>T (p.Q2469X) in exon 60 (Figure 1 and Figure 2A). The mouse *Fbn1* gene (GenBank accession number NM_007993.2; Ensembl ENSMUSG00000027204) is located on chromosome 2 and contains 66 exons, with the ATG start codon in exon 2 and the TAA stop codon in exon 66.

The *Fbn1*^{Q2469X} allele was generated using CRISPR/Cas9-mediated genome editing (Cyagen Biosciences, Santa Clara, CA). Cas9 mRNA, sgRNA, and a donor oligonucleotide

carrying the Q2469X mutation (CAG>TAG) were co-injected into zygotes. Homology-directed repair introduced the nonsense mutation into exon 60, and a silent mutation (TCC>TCG) was incorporated to prevent re-cutting by sgRNA. Pups were genotyped by PCR and confirmed by Sanger sequencing. Positive founders were bred to establish germline transmission. Sequence analysis of five predicted off-target sites showed no evidence of unintended mutations. Wild-type DNA was sequenced in parallel as a negative control to exclude artifacts from sequencing chromatograms.

The resulting *Fbn1*$^{Q2469X/+}$ line was designated as *Fbn1*^{tmQ2469XWSUlili} (abbreviated *Fbn1*$^{Q2469X/+}$ or FBN1Q2469X when deposited at The Jackson Laboratory), following the official guidelines for mouse strain nomenclature (http://www.informatics.jax.org/mgihome/nomen/gene.shtml).

All animal procedures were approved by the Institutional Animal Care and Use Committee (IACUC) of Wayne State University (WSU) and conformed to the NIH Guide for the Care and Use of Laboratory Animals. The *Fbn1*$^{Q2469X/+}$ mice were maintained on a C57BL/6J background, and both sexes were used in experiments.

Mouse Genotyping Genomic DNA was isolated from pup toes or adult ear punches using DirectPCR lysis buffer (Viagen Biotech) supplemented with Proteinase K (10 mg/mL). Samples were digested overnight at 55 °C, followed by heat inactivation at 98 °C for 10 minutes. PCR amplification was performed using REDTaq ReadyMix (Sigma-Aldrich) with the following primers: forward 5′-AACAGGGACCGCCTGTGTAGGTAG-3′ and reverse 5′-GCTCAGGGTTATCCTCAGGGACC-3′, yielding a 492 bp product. PCR conditions were: initial denaturation at 95 °C for 1 minute; 35 cycles of denaturation at 95 °C for 10 seconds, annealing at 62 °C for 30 seconds, and extension at 72 °C for 30 seconds; and a final extension at 72 °C for 10 minutes.

The *Fbn1*$^{Q2469X/+}$ allele introduces a SpeI restriction site (ACTAGT), allowing differentiation of wild-type (492 bp), *Fbn1*$^{Q2469X/+}$ heterozygous (492 bp, 305 bp and 187 bp), and *Fbn1*$^{Q2469X/Q2469X}$ homozygous (305 bp and 187 bp) genotypes. PCR products were digested with SpeI (New England Biolabs) in a 15 µL reaction containing 1.5 µL CutSmart buffer, 3 \µL ddH_2O, and 0.5 µL SpeI enzyme per reaction. Five microliters of the digestion mix was added to 10 µL PCR product and incubated at 37 °C for 3 hours. Digested fragments were resolved a 1.5% agarose gel in TBE buffer at 100 V for 30 minutes and visualized by ethidium bromide staining (Figure 2B).

High-fat diet (HFD)Treatment All procedures were approved by the Institutional Animal Care and Use Committee (IACUC) of Wayne State University. Beginning at 6 weeks of age, *Fbn1*$^{Q2469X/+}$ mice and their wild-type littermates were fed either a high-fat diet (HFD; 60 kcal% fat, Research Diets, Cat. #D12492) or a standard chow diet (SD; LabDiet, Cat. #5L0D) for 24 weeks.

Sequence Verification of the *Fbn1* Mutation The presence of the FBN1 mutation was verified by Sanger sequencing (GENEWIZ). PCR products amplified with primers flanking the Q2467X site (Table 1) were submitted together with 40 µl of 5 µM forward and reverse primers. Forward and reverse reads were aligned to the *FBN1* reference sequence using NCBI BLAST (nucleotide database). Sequences were examined for the wild-type allele (CATTGTTCC) or the mutant allele (TAGTGTTCG). Sequence trace files were visualized using Chromas Lite software to generate chromatograms for DNA and cDNA. Representative chromatograms are shown for a Marfan patient carrying the FBN1Q2467X mutation and for mice of three genotypes (*Fbn1*$^{+/+}$, *Fbn1*$^{Q2469X/+}$ and *Fbn1*$^{Q2469X/Q2469X}$)(Figure 1B, Figure 2B, 2D).

Table 1. Primers used to sequence *FBN1* gene and cDNA		
Species	**Primer name**	**oliogo sequence**
Human	*FBN1*DNA-F	5'- AGCACAGGACAATCATCAA -3'
	*FBN1*DNA-R	5'- AGTTCTTACAGGCAAAGGA -3'
	*FBN1*cDNA-F	5'- GACAGAGGATCATATCATTGC -3'
	*FBN1*cDNA-R	5'CAGTTGTGTTGCTTGGTT -3'
Mouse	*Fbn1*cDNA-F	5'-ATGGGGAGTGTGTCAACGAC-3'
	*Fbn1*cDNA-R	5'- GGCATTTGCATGTGAAGCCA-3'

Blood Pressure Measurement Systolic blood pressure was measured in both $Fbn1^{+/+}$ and $Fbn1^{Q2469X/+}$ mice at 3 months of age using the CODA™ Non-Invasive Blood Pressure System (Kent Scientific, Torrington, CT). Mice underwent a 10-day testing protocol, with a 2-day rest period between two 5-day sessions. The first 5 days were used to acclimate the animals to the holders and equipment, and the subsequent 5 days were used for data collection. Blood pressure values were averaged across the final 5-day recording period. Equipment performance and signal quality were monitored continuously, and measurements were repeated if artifacts or cuff malfunctions were detected.

Echocardiography Adult $Fbn1^{+/+}$ and $Fbn1^{+/Q2469X}$ mice were assessed by transthoracic echocardiography using the Vevo 3100 system equipped with an MS550 transducer, as previously described [19].Mice were anesthetized with 3% isoflurane in oxygen for induction and maintained at 1.5–2% isoflurane during imaging. Animals were positioned supine on a heated platform, and aortic dimensions were measured at the aortic root and ascending aorta. Vessel mechanical properties were derived from echocardiographic recordings.

Latex Injection for Aneurysm Visualization To visualize aortic morphology during aneurysm progression, vascular casting with yellow latex was performed as previously described [20] with modifications. After euthanasia, the abdominal and thoracic cavities were opened to expose the heart and major vessels. The right atrium was incised following perfusion with PBS through the left ventricle. To preserve native aortic morphology, PBS was replaced with 4% neutral-buffered formalin for fixation. Two milliliters of yellow latex medium (Ward's Science, catalog #470024-616) were then slowly injected through the left ventricle. The left ventricle and right atrium were clamped with Serrefine clamps, and mice were immersed in 4% neutral-buffered formalin overnight at 4 °C. The following day, formalin was replaced with 70% ethanol for ~2 hours at 4 °C before dissection and imaging.

Aorta Isolation and Processing for RNA-seq, Western Blotting, and Histology $Fbn1^{+/+}$ and $Fbn1^{Q2469X/Q2469X}$ mice at 13–15 days of age were euthanized, and the thoracic cavity was opened. The right atrium was incised to allow blood drainage, followed by perfusion with ice-cold PBS through the left ventricle until the effluent was clear and the liver appeared pale. Perfusion was then continued with 4% paraformaldehyde (PFA) to fix the aorta *in situ*. Hearts and aortas were collected, post-fixed in 4% PFA for 8–12 hours at 4 °C, and cryoprotected in 30% sucrose at 4 °C overnight or until tissues reached equilibrium (floating midway in solution). Tissues were embedded in OCT compound on dry ice and stored at −80 °C. Cryosections were cut at 5 *μm* thickness and mounted onto glass slides, which were stored at −20 °C until use.

Histology analyses OCT-embedded aortic sections (5 *μm*) were used for hematoxylin and eosin (H&E), collagen (Picro Sirius Red Stain Kit, Abcam, Cat. #ab150681), and elastic fiber staining (Verhoeff–Van Gieson Elastin Kit, Polysciences, Cat. #25089). Prior to staining, three preparatory

steps were performed: (1) slides were removed from the −20 °C freezer and allowed to equilibrate at room temperature for 30 minutes; (2) sections were fixed in cold methanol:acetone (1:1) for 5 minutes; and (3) slides were rinsed twice in PBS (3 minutes each). Stained sections were imaged by light microscopy using a Leica DM4000B microscope and LAS software at 400× magnification. Multiple images were acquired and stitched digitally to generate high-resolution composite images.

Immunofluorescence OCT-embedded aortic sections (5 *μm)* were air-dried for 30 minutes at room temperature, fixed in cold acetone:methanol (1:1) for 10 minutes, and rinsed in PBS. Sections were permeabilized with 0.1% Triton X-100 in PBS (2 × 5 minutes), followed by washing in PBST (0.1% Tween-20 in PBS). Endogenous peroxidase activity was quenched with 3% H_2O_2 in methanol (10 minutes), and sections were rinsed again in PBST (3 × 5 minutes). Tissue boundaries were circled with a hydrophobic barrier pen, and sections were blocked with PBS containing 10% serum (matched to the host species of the secondary antibody) and 1% BSA for 1 hour. Slides were incubated overnight at 4 °C with primary antibodies diluted in 50% blocking buffer. After washing (3 × 5 minutes, PBST), sections were incubated with secondary antibodies (diluted in 50% blocking buffer) for 2 hours at room temperature, followed by additional washes (5 × 5 minutes, PBST). Sections were dehydrated in graded ethanol (95% for 20 seconds, 100% twice for 30 seconds each), cleared in xylene (3 × 1 minute), and mounted with DAPI-containing medium (Vector Laboratories, Cat. #H-2000). Fluorescence images were captured using a Leica DM4000B microscope with LAS software at 400× magnification. Multiple fields were acquired per section. All antibodies were tested in triplicate, and negative controls omitting the primary antibody were included in each experiment.

RNA extraction for RNA-seq and qPCR Thoracic aorta **from** *Fbn1*$^{+/+}$, *Fbn1*$^{Q2469X/+}$ and *Fbn1*$^{Q2469X/Q2469X}$ mice at 13 day old pups (n=3) were isolated and preserved in RNAlater and store in -70^{0}C. RNA extraction, library preparation, RNA-seq and transcriptome analysis was performed by Admera Health Inc. (New Jersey, United States): sample were isolated using Qiagen RNeasy Plus Micro Kit (Qiagen, Hilden, Germany) with a modified protocol. RNA sample quality was assessed by Agilent RNA 6000 Pico Reagent on Agilent 2100 Bioanalyzer (Agilent Technologies, Santa Clara, CA) and quantified by Qubit RNA HS assay (ThermoFisher, Waltham, MA). Ribosomal RNA depletion and library preparation was performed for each sample with TruSeq Stranded Total RNA Library Prep Gold (Illumina Inc., San Diego, CA), following manufacturer's instructions. Average final library size is about 300 bp. Illumina 8-nt dual-indices were used for multiplexing. Samples were pooled and sequenced on Illumina HiSeq X sequencer for 150 bp read length in paired-end mode, with an output of 80 million reads per sample (40M reads in each direction).

RNA extraction from aorta tissues (**flash freeze in liquid N2 and stored at -70^{0}C**). cDNA for qPCR was synthesized using Superscript III reverse transcriptase (Invitrogen). Real-time PCR was performed using the Step-One Plus system (Applied Biosystems) in the presence of SYBR Green. *Gapdh* and *U6* was used as internal control. Changes in mRNA expression were expressed as fold change relative to internal control. All gene specific PCR primers were designed to flank at least 2 exons (Table 2).

RNA-seq Analyses RNA sequencing was performed by Admera Health Inc. Quality of raw reads was assessed using FastQC (v0.11.8). Adapter sequences and low-quality bases were trimmed with Trimmomatic (v0.38). Clean reads were aligned to the human reference genome (hg38) using STAR Aligner (v2.7.1a). Gene-level reading counts were obtained with HTSeq-count (v0.11.2). Mapping quality was evaluated with Picard tools (v2.20.4; https://broadinstitute.github.io/picard/). Transcript abundances were estimated as fragments per kilobase per million mapped reads (FPKM) using StringTie (v2.0.4).
Differential gene expression analysis was performed with DESeq2. Raw count data were normalized using the variance stabilizing transformation (VST) implemented in DESeq2 to obtain

homoscedastic, log2-scale expression values. The top 2,000 most variable genes across samples were selected for heatmap visualization. For each gene, expression values were mean-centered to generate z-scores, which determined the heatmap color gradient. VST-normalized values were also used to compute pairwise Pearson correlations between samples. Sample distance heatmaps were constructed using the distance metric $\sqrt{(1 - r^2)}$, where *r* is the Pearson correlation coefficient.

Protein Extraction and Western Blotting Thoracic aortas were collected from 13-day-old *Fbn1*$^{+/+}$ *Fbn1*$^{Q2469X/+}$ and *Fbn1*$^{Q2469X/Q2469X}$ mice (n = 3 per group). Protein lysates were prepared, and concentrations were determined using the BCA assay (Thermo Fisher Scientific). Equal amounts of protein were separated on 4–12% Bis–Tris NuPAGE Mini Gels (Invitrogen) and transferred onto PVDF membranes (Millipore) using the XCell II Blot Module (Invitrogen). A Spectra™ Multicolor Broad Range Protein Ladder (Thermo Fisher Scientific, Cat. #26634) was included for molecular weight estimation. Membranes were blocked with 5% nonfat milk at room temperature for 1 hour and incubated overnight at 4 °C with primary antibodies against fibrillin-1 (Abcam, Cat. #ab231094, 0.2 µg/mL; ~312 kDa) and vinculin (Santa Cruz, Cat. #sc73614, 1:100; ~117 kDa). After washing, membranes were incubated with HRP-conjugated secondary antibodies (anti-rabbit IgG, Abcam, Cat. #ab6721, 1:2000; anti-mouse IgG, Sigma-Aldrich, Cat. #AP130, 1:3000) for 1.5 hours at room temperature. Signals were detected by enhanced chemiluminescence (SuperSignal West Pico Chemiluminescent Substrate, Thermo Fisher Scientific, Cat. #21050) and imaged using the KwikQuant Imager (Kindle Biosciences).

Statistical analyses To Observed genotype frequencies were compared with expected Mendelian ratios using the chi-square test. Survival of *Fbn1*$^{Q2469X/Q2469X}$ mice was assessed by Kaplan–Meier analysis, and survival curves were compared using the log-rank test. Group comparisons were performed using two-tailed Student's *t* tests. All statistical analyses were conducted with GraphPad Prism 9 (GraphPad Software, San Diego, CA). Data are presented as mean ± SEM, and the number of experimental replicates is provided in the figure legends. A *P* value < 0.05 was considered statistically significant.

Results

The *FBN1Q2467X* nonsense mutation in Marfan patients is associated with reduced fibrillin-1 expression Typically, MFS patients first present with aneurysms at the aortic root and ascending aorta that require surgical repair[5]. In the case shown here, a MFS patient with the *FBN1* c.7399C>T (p.Q2467X) mutation developed additional aneurysms in the aortic arch following repair of the aortic root and ascending aorta (Figure 1A). Sequence chromatogram analysis of DNA and RNA isolated from aneurysm tissue confirmed the presence of the mutation. Genomic DNA revealed heterozygosity at nucleotide position c.7399 (C/T), whereas cDNA from the same tissue showed only the wild-type C allele, indicating selective degradation of the mutant transcript by nonsense-mediated decay (Figure 1B). Consistent with this, qPCR and Western blot analyses demonstrated ~50% reductions in *FBN1* mRNA and protein expression in the patient sample compared with a non-Marfan control.

The *FBN1* gene is located on chromosome 15q21.1 and comprises 66 exons encoding a 9,847 bp mRNA and a fibrillin-1 protein of 2,873 amino acids (~350 kDa) (Table S1). Genetic testing of MFS patients has identified a c.7399C>T transition in exon 59, which converts the CAG codon for glutamine (Q2467) into a premature stop codon (TAG), generating the *FBN1Q2467X* nonsense mutation [17,18]. This mutation lies within the calcium-binding epidermal growth factor–like domain 39 (Figure 1C).

CRISPR/Cas9-mediated generation of a Marfan mouse model carrying the orthologous *Fbn1Q2469X* mutation *FBN1* gene is highly conserved between human and mouse with 96% conservation in protein identity and 98% in protein similarity (Table S1). To model the human

FBN1Q2467X nonsense mutation, we used CRISPR/Cas9 genome editing to introduce the orthologous mutation (*c.7405C>T,* Q2469X) into the mouse *Fbn1* gene (Figure 2A). The resulting *Fbn1*$^{Q2469X/+}$ mice bred to produce *Fbn1*$^{+/+}$, *Fbn1*$^{Q2469X/+}$ and *Fbn1*$^{Q2469X/Q2469X}$ mouse at Mendelian ratio. Although *Fbn1*$^{Q2469X/Q2469X}$ mouse is indistinguishable from the littermates at birth, some *Fbn1*$^{Q2469X/Q2469X}$ mice were runted at 10 days after birth and displayed early lethality (Figure. 2A).

Since the C to T mutation creates a Spe1 restriction site that is only present in the *Fbn1* mutant allele. Genotyping was confirmed by PCR amplification of the target locus followed by SpeI digestion, which distinguishes the wild-type allele (492 bp) from the mutant allele (307 and 187 bp fragments). Sanger sequencing further validated the presence of the c.7405C>T mutation in heterozygous and homozygous mice (Figure 2B).

A nonsense mutation in *Fbn1* could either generate a truncated fibrillin-1 protein or trigger selective degradation of mutant transcripts via nonsense-mediated decay (NMD), resulting in FBN1 deficiency. To distinguish between these possibilities, we assessed *Fbn1* expression in mouse aortas, qPCR revealed that *Fbn1* mRNA levels were reduced by ~50% in heterozygotes and by ~95% in homozygotes compared with wild-type littermates (Figure 2C). Sequencing of RT-PCR products demonstrated that only the wild-type C nucleotide, and not the mutant T, was detected in heterozygotes, indicating loss of mutant transcripts (Figure 2D). The near-complete reduction of *Fbn1* mRNA and the absence of detectable fibrillin-1 protein in homozygotes further support NMD-mediated transcript degradation. These findings confirm that the *Fbn1Q2469X* nonsense mutation leads to FBN1 deficiency, rather than the production of truncated protein, in both heterozygous and homozygous mice.

Western blotting demonstrated a gene dosage–dependent reduction of fibrillin-1 protein: modestly decreased in heterozygotes and severely decreased in homozygotes compared with wild-type controls. Vinculin was used as a loading control (Figure 2E). *Together, these data establish that the Fbn1Q2469X allele induces haploinsufficiency through nonsense-mediated decay: providing a faithful genetic model of the human FBN1Q2467X mutation.*

***Fbn1*$^{Q2469X/+}$ mice appear normal but are susceptible to aortic dilation at the root and ascending aorta in response to HFD treatment.** *Fbn1*$^{Q2469X/+}$ mice appear grossly normal, indistinguishable from their wild type littermates. There is no significant aorta dilation and rupture within the first year of mouse life. Although echocardiogram shows a slight dilation of the aorta root (L1, L2, L3) and the ascending aorta in *Fbn1*$^{Q2469X/+}$ mice (Figure 3A), the increase is not statistically significant (Figure 3B). Compared with the wild type of littermate controls, *Fbn1*$^{Q2469X/+}$ mice show slightly decreased blood pressure: however, the decrease is not of statistical significance for both systolic and diastolic blood pressure (P = 0.066 and P=0.4831 respectively) for male and female mice (Figure. S1). Histology analyses of the aorta in *Fbn1*$^{Q2469X/+}$ mice shows normal morphology with smooth muscle cell alignment, collagen expression level and intact elastin fibers (data not shown).

To examine the response of *Fbn1*$^{Q2469X/+}$ mice to metabolic stress, we treated the mice with HFD for 6 months. High-fat diet significantly induces aortic dilation in the aortic root and the ascending aorta of *Fbn1*$^{Q2469X/+}$ mice by latex injection; histology analyses including H&E and elastic fiber staining show significant VSMC disorganization and elastic fiber fragmentation Figure 3C). The echocardiogram shows significant aortic dilation at L1, L2, L3 and ascending aorta (Figure 3D). These results demonstrate that the FBN1Q2469X mutation is pathogenic, making mice vulnerable to metabolic stress such as HFD.

***Fbn1*$^{Q2469X/Q2469X}$ mice develop progressive thoracic aortic aneurysms, leading to sudden death due to aneurysm rupture** The *Fbn1*$^{Q2469X/Q2469X}$ mice all die out within 25 days after birth while the littermate *Fbn1*$^{+/+}$ and *Fbn1*$^{Q2469X/+}$ mice are alive during the time. To visualize aneurysm progression at different time after birth, we performed latex injection in *Fbn1*$^{Q2469X/Q2469X}$ mice (Figure 4A). We do not observe apparent difference among littermates with different genotypes

from P0-P5 after birth. The dilation of the aortic root and ascending aorta dilation is observed at P7 after birth (Figure. 4A Early stage). The dilation progress to rupture is observed at P13 at the aortic root, ascending aorta-arch region (Figure 4A, late stage). The aneurysm rupture is observed at P13 at the junction of ascending aorta (Figure 4A, right side perfused by PBS).

To determine the mortality rate of *Fbn1*$^{Q2469X/Q2469X}$ mice, we performed Kaplan-Meier survival curve analyses of *Fbn1*$^{+/+}$, *Fbn1*$^{Q2469X/+}$ and *Fbn1*$^{Q2469X/Q2469X}$ mice, and the log-rank test determines the statistical significance between *Fbn1*$^{Q2469X/Q2469X}$ mice and *Fbn1*$^{+/+}$ or *Fbn1*$^{Q2469X/+}$ mice (n=30 for each genotype, $P<0.0001$): all of the *Fbn1*$^{Q2469X/Q2469X}$ mice die of aneurysm rupture within 25 days, and most of these mice die between 13-15 days after birth (Figure 4B). All *Fbn1*$^{Q2469X/Q2469X}$ mice die from hemothorax with blood clots filled lung and the rupture of thoracic aortic aneurysm. Sex does not affect the survival of *Fbn1*$^{Q2469X/Q2469X}$ mice (Figure 4C).

To investigate the molecular changes of the vessel wall during aneurysm progression to rupture, we conducted histological analyses using HE stain, Picru Sirius Red connective tissue stain and Verhoeff Van Gieson Elastin Stain on the thoracic aortic sections of the aneurysms at both early and late stages (Figure 4D). We observed that (1) the vessel wall of aneurysms is thickened at early stage and degenerated at late stage; (2) the smooth muscle layer of the aorta wall become disorganized in *Fbn1*$^{Q2469X/Q2469X}$ mice comparing with the elongated SMC arrays in the wild type mice; (3) the cell loss is apparent at the late stage; (4) Picru Sirius Red connective tissue staining shows no significant changes in collagen in early-stage aneurysms, but drastic collagen degradation in late-stage aneurysms; (4) Verhoeff Van Gieson Elastin Stain detects amorphous elastic fibers at early stage and severe fragmentation and degradation at late stage in *Fbn1*$^{Q2469X/Q2469X}$ mice, not in the wild type littermates. Despite widespread *FBN1* expression, histological examination of systemic organs, including heart, liver, kidney, skeletal muscle, and lung, revealed no major abnormalities in *Fbn1*$^{Q2469X/Q2469X}$ mice at day 13, indicating that pathology at this stage is largely confined to the aorta (Figure S2) These results collectively demonstrate the pathological changes including VSMC dedifferentiation, collagen degradation and elastin fragmentation during aneurysm progression in *Fbn1*$^{Q2469X/Q2469X}$ mice during aneurysm progression.

Inflammation and immune response are the predominant pathogenic processes in *Fbn1*$^{Q2469X/Q2469X}$ aneurysms To explore the molecular drivers of aneurysm progression to rupture, we performed bulk RNA-seq analyses of thoracic aortas from *Fbn1*$^{Q2469X/Q2469X}$ mice and wild-type (WT) littermates (n=3 per group; Figure 5A). Hierarchical clustering revealed distinct transcriptomic patterns between genotypes under a threshold of $P<0.01$ (Figure 5B). Using established criteria (fold change >2.0, $P<0.01$, FDR<0.05), we identified 854 differentially expressed genes (DEGs), including 643 upregulated and 211 downregulated transcripts in *Fbn1Q2469X/Q2469X* mice (Table S2–S3).

A volcano plot highlighted significantly altered DEGs between mutant and WT aortas, including genes associated with immune response, thrombosis, vascular remodeling, and extracellular matrix turnover, such as *F5, F10, Arg1, A2M, Thbs1, Itgam, Igfbp2, C6, Retnla,* and *ADAMTS16* (Figure 5C). Gene Ontology (GO) enrichment analysis of DEGs identified 148 biological process, 10 molecular function, and 21 cellular component terms (Table S4). The top 20 enriched GO terms (adjusted $P<0.05$) included cytokine-mediated signaling pathways and inflammatory responses as the most significantly altered categories during aneurysm progression and rupture (Figure 5D).

KEGG pathway analysis revealed enrichment of 29 pathways among upregulated DEGs and 3 pathways among downregulated DEGs (Figure S3; Table S5). Cytokine–cytokine receptor interaction and primary immunodeficiency were the most significantly enriched pathways in upregulated and downregulated DEGs, respectively (adjusted $P<0.05$). Together, these transcriptomic analyses highlight inflammation and immune activation as the predominant pathogenic processes driving aneurysm progression in *Fbn1*$^{Q2469X/Q2469X}$ mice (Table S6).

Gene Ontology enrichment highlights inflammatory signaling in aneurysms of *Fbn1*$^{Q2469X/Q2469X}$ mice To further define the biological processes underlying the transcriptomic changes observed in aneurysms of *Fbn1*$^{Q2469X/Q2469X}$ mice, we performed Gene Ontology (GO) enrichment analysis on the differentially expressed genes (DEGs) identified by RNA-seq. A chord diagram illustrated the top 10 enriched GO terms and their associated DEGs, with upregulated genes (red) and downregulated genes (purple) mapped to functional categories such as cytokine signaling, immune activation, and extracellular matrix organization (Figure 6A).

A circular plot analysis of the top 10 inflammation-related GO terms further emphasized immune signaling as a central feature of the transcriptomic profile (Figure 6B). Upregulated genes were prominently linked to pathways involved in cytokine-mediated signaling, leukocyte activation, and response to wounding. The z-score distribution indicated that most inflammatory pathways were activated in aneurysms of *Fbn1*$^{Q2469X/Q2469X}$ mice, with pathway significance reflected by circle size (P<0.05). Together, these analyses highlight inflammation as a dominant biological process in aneurysm progression, building upon the global transcriptomic analyses (Figure 5).

Adventitial inflammation increases with aneurysm progression To confirm the presence of immune cell infiltration marked by CD11B in aneurysms, we performed immunofluorescent staining on OCT sections from the thoracic aorta of *Fbn1*$^{Q2469X/Q2469X}$ mice at early, intermediate and late stages. Immunofluorescence staining reveals the spatial distribution of immune cells in the vessel wall: aneurysmal vs nonaneurysmal area; few immune cells are detected in the endothelial nor VSMCs, most immune cells are located in the adventitia area. These results demonstrated a progressive increase in adventitial immune cell infiltration as aneurysms advanced from early to late stages. At the early stage, few CD11B$^+$ cells were observed in the aneurysmal vessel wall. By the intermediate stage, CD11B$^+$ cells became localized primarily to the adventitia of the aneurysmal region. At the late stage, CD11B$^+$ signals were markedly elevated, with dense accumulation particularly in the adventitia near rupture sites (Figure 7).

This stepwise increase in adventitial immune cell infiltration suggests that inflammation in the outer vessel wall is not simply a secondary byproduct of rupture but is closely associated with the pathological remodeling that drives aneurysm progression. The pattern of CD11B$^+$ cell accumulation highlights the adventitia as a critical site of immune activation in Marfan-associated aneurysms and supports the concept that adventitial inflammation contributes to the transition from stable aneurysm to rupture-prone disease.

Discussion

Summary of key findings In this study, we demonstrated that the FBN1Q2467X nonsense mutation identified in Marfan patients results in fibrillin-1 deficiency due to nonsense-mediated decay, rather than production of a truncated protein (Figure 1). Using CRISPR/Cas9, we generated a knock-in *Fbn1*$^{+/Q2469X}$ mouse model carrying the patient-derived mutation, which likewise causes haploinsufficiency through mRNA degradation (Figure 2). Heterozygous mice displayed only mild aortic dilation under baseline conditions, but high-fat diet feeding induced aneurysm formation in the aortic root and ascending aorta, progressing to rupture (Figure 3). In contrast, homozygous mice developed rapidly progressive, fully penetrant thoracic aortic aneurysms that ruptured within 25 days (Figure 4). Histological analyses revealed smooth muscle cell remodeling, collagen degradation, and elastic fiber fragmentation (Figure 4D). Transcriptomic profiling identified inflammation and immune responses as the predominant biological processes in aneurysmal tissue (Figures 5–6). Immunofluorescence localized immune cell infiltration specifically to the adventitia at late stages near rupture (Figure 7). Together, these findings establish a rupture-prone model that faithfully recapitulates key pathogenic features of Marfan aneurysms and provide a valuable platform for mechanistic studies and therapeutic discovery (Figure 8).

Mutation-specific mechanisms and precision medicine FBN1 is a multifunctional glycoprotein that not only contributes to the structural integrity of microfibrils but also regulates critical signaling pathways, including TGF-β, integrins, and growth factor bioavailability [7,21,22]. Clinical evidence indicates that patients with different classes of *FBN1* mutations—missense, nonsense, frameshift, or splicing—exhibit overlapping yet distinct phenotypes and drug response. Notably, haploinsufficiency mutations, including nonsense variants, are associated with more severe aortic phenotypes and show a greater therapeutic response to Losartan, whereas patients carrying certain missense mutations respond poorly [9-14]. These genotype–phenotype correlations suggest that understanding the mechanistic consequences of individual mutation classes is essential for developing precision medicine strategies in Marfan syndrome.

Contributions of current and new mouse models Existing Marfan mouse models have substantially advanced our understanding of aneurysm formation [21,23], but each carries inherent limitations. The *Fbn1*$^{C1041G/+}$ knock-in model carries a patient-derived missense mutation and exhibits only mild aorta dilation without rupture [15]., limiting its utility for studying late-stage disease. The *Fbn1*$^{mgR/mgR}$ hypomorphic model, generated by an ES cell abnormal recombination event, reduces *fibrillin-1* expression but does not represent a clinically validated mutation [16]. Complete *Fbn1* knockout mice die shortly after birth [24]. Although their short lifespan resembles that of our homozygous *Fbn1*$^{Q2469X/Q2469X}$ mice, the underlying mechanism differs: our homozygotes retain ~10% residual F*bn1* mRNA due to incomplete nonsense-mediated decay (Figure 2C), which permits aneurysm formation and progresses to rupture (Figure 4). Histological examination of systemic organs at day 13 showed no major abnormalities, suggesting that pathology is largely confined to the aorta (Figure S2). This model therefore provides a consistent system to study aneurysm progression and rupture.

In contrast to the established *Fbn1* knockout models, the *Fbn1*$^{+/Q2469X}$ mice represent a bona fide patient-derived nonsense mutation that undergoes nonsense-mediated mRNA decay, faithfully modeling the haploinsufficiency class of human FBN1 mutations. Importantly, this model exhibits consistent and predictable rupture, offering a robust system to study both genetic and environmental modifiers of aneurysm progression and to test therapeutic strategies in the context of clinically relevant mutation biology.

Inflammation as a central and stage-specific process The role of inflammation in Marfan aneurysms has been debated, with some reports describing minimal immune involvement [25,26]. Our results challenge this view by demonstrating that inflammation is the predominant biological process at late stages of disease. Bulk RNA-seq revealed strong enrichment of cytokine-mediated signaling, leukocyte activation, and immune pathways, while immunofluorescence confirmed that CD11B^{+} immune cell infiltration is progressively localized to the adventitia near rupture. These findings suggest that adventitial inflammation is not an early initiating event but rather a critical accelerator of aneurysm progression and rupture. Future work will focus on dissecting the mechanisms that regulate this outside-in inflammatory response, including potential cross-talk between endothelial dysfunction, smooth muscle cell reorganization, and adventitial immune activation.

Translational implications and conclusion Consistent with our findings (Figures 5–6), recent transcriptomic and bioinformatics analyses of human Marfan aneurysms and experimental models have identified shared pathogenic signatures, including inflammation, oxidative stress, metabolic dysfunction, and mitochondrial impairment [27-29]. The central role of nonsense-mediated mRNA decay (NMD) in shaping *FBN1* haploinsufficiency aligns with broader work in RNA surveillance[30]. Our *Fbn1*$^{+/Q2469X}$ model complements these efforts by providing a consistent and reliable platform to study the late stages of aneurysm progression. This model enables the identification of biomarkers associated with rupture risk and serves as a preclinical system to evaluate anti-inflammatory and metabolic therapies. By linking patient-derived nonsense

mutations to experimental biology, the *Fbn1*$^{+/Q2469X}$ mouse offers a valuable translational tool for mechanistic studies and drug discovery in Marfan syndrome and related thoracic aortic aneurysms.

Acknowledgments This project was initiated upon the suggestion and encouragement of Dr. Lynne Maquat (University of Rochester). Her insights into nonsense-mediated decay were instrumental in our pursuing the generation of a Marfan mouse model carrying a FBN1 nonsense mutation. We would like to thank the excellent technique assistance from people working in the lab and help discussions from colleagues during the course of this study. We are grateful for the aneurysm tissues of Marfan patient from the Biobank of University of Michigan. This work was supported by funding from the WSU OVPR Grant Boost Award, the National Heart, Lung, and Blood Institute (HL119815, HL142956 to L.L.).

Author contributions

S.W., J.Z. A.P. and L.L. conceived and designed the experiments; S.W., J.Z. A.P, D. J., M.Y., performed the experiments; S.W., J.Z. A.P, D. J., M.Y., D.X., C.L., L.L., Y.X., K.Z., H.L., Z.Y. and L.L. analyzed the data; S.W., J.Z. A.P., K.Z., Y.X. and L.L. wrote and revised the manuscript. All authors approved the manuscript.

Data availability All of original data are available upon request.

Additional information The authors declare no competing financial and non-financial interests.

1. McKusick VA. The defect in Marfan syndrome. *Nature*. 1991;352:279–281. doi: 10.1038/352279a0
2. Dietz HC, Cutting GR, Pyeritz RE, Maslen CL, Sakai LY, Corson GM, Puffenberger EG, Hamosh A, Nanthakumar EJ, Curristin SM, et al. Marfan syndrome caused by a recurrent de novo missense mutation in the fibrillin gene. *Nature*. 1991;352:337–339. doi: 10.1038/352337a0
3. Roman MJ, Rosen SE, Kramer-Fox R, Devereux RB. Prognostic significance of the pattern of aortic root dilation in the Marfan syndrome. *J Am Coll Cardiol*. 1993;22:1470–1476. doi: 10.1016/0735-1097(93)90559-j
4. Milewicz DM, Braverman AC, De Backer J, Morris SA, Boileau C, Maumenee IH, Jondeau G, Evangelista A, Pyeritz RE. Marfan syndrome. *Nat Rev Dis Primers*. 2021;7:64. doi: 10.1038/s41572-021-00298-7
5. Isselbacher EM, Preventza O, Hamilton Black Iii J, Augoustides JG, Beck AW, Bolen MA, Braverman AC, Bray BE, Brown-Zimmerman MM, Chen EP, et al. 2022 ACC/AHA Guideline for the Diagnosis and Management of Aortic Disease: A Report of the American Heart Association/American College of Cardiology Joint Committee on Clinical Practice Guidelines. *J Am Coll Cardiol*. 2022;80:e223–e393. doi: 10.1016/j.jacc.2022.08.004
6. Sakai LY, Keene DR, Engvall E. Fibrillin, a new 350-kD glycoprotein, is a component of extracellular microfibrils. *J Cell Biol*. 1986;103:2499–2509.
7. Sakai LY, Keene DR, Renard M, De Backer J. FBN1: The disease-causing gene for Marfan syndrome and other genetic disorders. *Gene*. 2016;591:279–291. doi: 10.1016/j.gene.2016.07.033

8. Faivre L, Collod-Beroud G, Loeys BL, Child A, Binquet C, Gautier E, Callewaert B, Arbustini E, Mayer K, Arslan-Kirchner M, et al. Effect of mutation type and location on clinical outcome in 1,013 probands with Marfan syndrome or related phenotypes and FBN1 mutations: an international study. *Am J Hum Genet*. 2007;81:454–466. doi: 10.1086/520125
9. Franken R, Teixido-Tura G, Brion M, Forteza A, Rodriguez-Palomares J, Gutierrez L, Garcia Dorado D, Pals G, Mulder BJ, Evangelista A. Relationship between fibrillin-1 genotype and severity of cardiovascular involvement in Marfan syndrome. *Heart*. 2017;103:1795–1799. doi: 10.1136/heartjnl-2016-310631
10. Xu S, Li L, Fu Y, Wang X, Sun H, Wang J, Han L, Wu Z, Liu Y, Zhu J, et al. Increased frequency of FBN1 frameshift and nonsense mutations in Marfan syndrome patients with aortic dissection. *Mol Genet Genomic Med*. 2020;8:e1041. doi: 10.1002/mgg3.1041
11. Franken R, den Hartog AW, Radonic T, Micha D, Maugeri A, van Dijk FS, Meijers-Heijboer HE, Timmermans J, Scholte AJ, van den Berg MP, et al. Beneficial Outcome of Losartan Therapy Depends on Type of FBN1 Mutation in Marfan Syndrome. *Circ Cardiovasc Genet*. 2015;8:383–388. doi: 10.1161/CIRCGENETICS.114.000950
12. Dietz HC. Potential Phenotype-Genotype Correlation in Marfan Syndrome: When Less is More? *Circ Cardiovasc Genet*. 2015;8:256–260. doi: 10.1161/CIRCGENETICS.115.001040
13. Takeda N, Inuzuka R, Maemura S, Morita H, Nawata K, Fujita D, Taniguchi Y, Yamauchi H, Yagi H, Kato M, et al. Impact of Pathogenic FBN1 Variant Types on the Progression of Aortic Disease in Patients With Marfan Syndrome. *Circ Genom Precis Med*. 2018;11:e002058. doi: 10.1161/CIRCGEN.117.002058
14. De Backer J, Campens L, Muino Mosquera L. Looking for the Missing Links: Challenges in the Search for Genotype-Phenotype Correlation in Marfan Syndrome. *Circ Genom Precis Med*. 2018;11:e002185. doi: 10.1161/CIRCGEN.118.002185
15. Judge DP, Biery NJ, Keene DR, Geubtner J, Myers L, Huso DL, Sakai LY, Dietz HC. Evidence for a critical contribution of haploinsufficiency in the complex pathogenesis of Marfan syndrome. *J Clin Invest*. 2004;114:172–181. doi: 10.1172/JCI20641
16. Pereira L, Lee SY, Gayraud B, Andrikopoulos K, Shapiro SD, Bunton T, Biery NJ, Dietz HC, Sakai LY, Ramirez F. Pathogenetic sequence for aneurysm revealed in mice underexpressing fibrillin-1. *Proc Natl Acad Sci U S A*. 1999;96:3819–3823.
17. Sakai H, Visser R, Ikegawa S, Ito E, Numabe H, Watanabe Y, Mikami H, Kondoh T, Kitoh H, Sugiyama R, et al. Comprehensive genetic analysis of relevant four genes in 49 patients with Marfan syndrome or Marfan-related phenotypes. *Am J Med Genet A*. 2006;140:1719–1725. doi: 10.1002/ajmg.a.31353
18. Turner CL, Emery H, Collins AL, Howarth RJ, Yearwood CM, Cross E, Duncan PJ, Bunyan DJ, Harvey JF, Foulds NC. Detection of 53 FBN1 mutations (41 novel and 12 recurrent) and genotype-phenotype correlations in 113 unrelated probands referred with Marfan syndrome, or a related fibrillinopathy. *Am J Med Genet A*. 2009;149A:161–170. doi: 10.1002/ajmg.a.32593
19. Lee L, Cui JZ, Cua M, Esfandiarei M, Sheng X, Chui WA, Xu MH, Sarunic MV, Beg MF, van Breemen C, et al. Aortic and Cardiac Structure and Function Using High-Resolution Echocardiography and Optical Coherence Tomography in a Mouse Model of Marfan Syndrome. *PLoS One*. 2016;11:e0164778. doi: 10.1371/journal.pone.0164778
20. Lee VS, Halabi CM, Hoffman EP, Carmichael N, Leshchiner I, Lian CG, Bierhals AJ, Vuzman D, Brigham Genomic M, Mecham RP, et al. Loss of function mutation in LOX causes thoracic aortic aneurysm and dissection in humans. *Proc Natl Acad Sci U S A*. 2016;113:8759–8764. doi: 10.1073/pnas.1601442113

21. Milewicz DM, Prakash SK, Ramirez F. Therapeutics Targeting Drivers of Thoracic Aortic Aneurysms and Acute Aortic Dissections: Insights from Predisposing Genes and Mouse Models. *Annu Rev Med*. 2017;68:51–67. doi: 10.1146/annurev-med-100415-022956
22. Seeburun S, Wu S, Hemani D, Pham L, Ju D, Xie Y, Kata P, Li L. Insights into elastic fiber fragmentation: Mechanisms and treatment of aortic aneurysm in Marfan syndrome. *Vascul Pharmacol*. 2023;153:107215. doi: 10.1016/j.vph.2023.107215
23. Milewicz DM, Ramirez F. Therapies for Thoracic Aortic Aneurysms and Acute Aortic Dissections. *Arterioscler Thromb Vasc Biol*. 2019;39:126–136. doi: 10.1161/ATVBAHA.118.310956
24. Pereira L, Andrikopoulos K, Tian J, Lee SY, Keene DR, Ono R, Reinhardt DP, Sakai LY, Biery NJ, Bunton T, et al. Targetting of the gene encoding fibrillin-1 recapitulates the vascular aspect of Marfan syndrome. *Nat Genet*. 1997;17:218–222. doi: 10.1038/ng1097-218
25. Pisano C, Balistreri CR, Ricasoli A, Ruvolo G. Cardiovascular Disease in Ageing: An Overview on Thoracic Aortic Aneurysm as an Emerging Inflammatory Disease. *Mediators Inflamm*. 2017;2017:1274034. doi: 10.1155/2017/1274034
26. Malecki C, Hambly BD, Jeremy RW, Robertson EN. The Role of Inflammation and Myeloperoxidase-Related Oxidative Stress in the Pathogenesis of Genetically Triggered Thoracic Aortic Aneurysms. *Int J Mol Sci*. 2020;21. doi: 10.3390/ijms21207678
27. Pedroza AJ, Tashima Y, Shad R, Cheng P, Wirka R, Churovich S, Nakamura K, Yokoyama N, Cui JZ, Iosef C, et al. Single-Cell Transcriptomic Profiling of Vascular Smooth Muscle Cell Phenotype Modulation in Marfan Syndrome Aortic Aneurysm. *Arterioscler Thromb Vasc Biol*. 2020;40:2195–2211. doi: 10.1161/ATVBAHA.120.314670
28. Li Y, Ren P, Dawson A, Vasquez HG, Ageedi W, Zhang C, Luo W, Chen R, Li Y, Kim S, et al. Single-Cell Transcriptome Analysis Reveals Dynamic Cell Populations and Differential Gene Expression Patterns in Control and Aneurysmal Human Aortic Tissue. *Circulation*. 2020;142:1374–1388. doi: 10.1161/CIRCULATIONAHA.120.046528
29. Sun Y, Asano K, Sedes L, Cantalupo A, Hansen J, Iyengar R, Walsh MJ, Ramirez F. Dissecting aortic aneurysm in Marfan syndrome is associated with losartan-sensitive transcriptomic modulation of aortic cells. *JCI Insight*. 2023;8. doi: 10.1172/jci.insight.168793
30. Kurosaki T, Popp MW, Maquat LE. Quality and quantity control of gene expression by nonsense-mediated mRNA decay. *Nat Rev Mol Cell Biol*. 2019;20:406–420. doi: 10.1038/s41580-019-0126-2

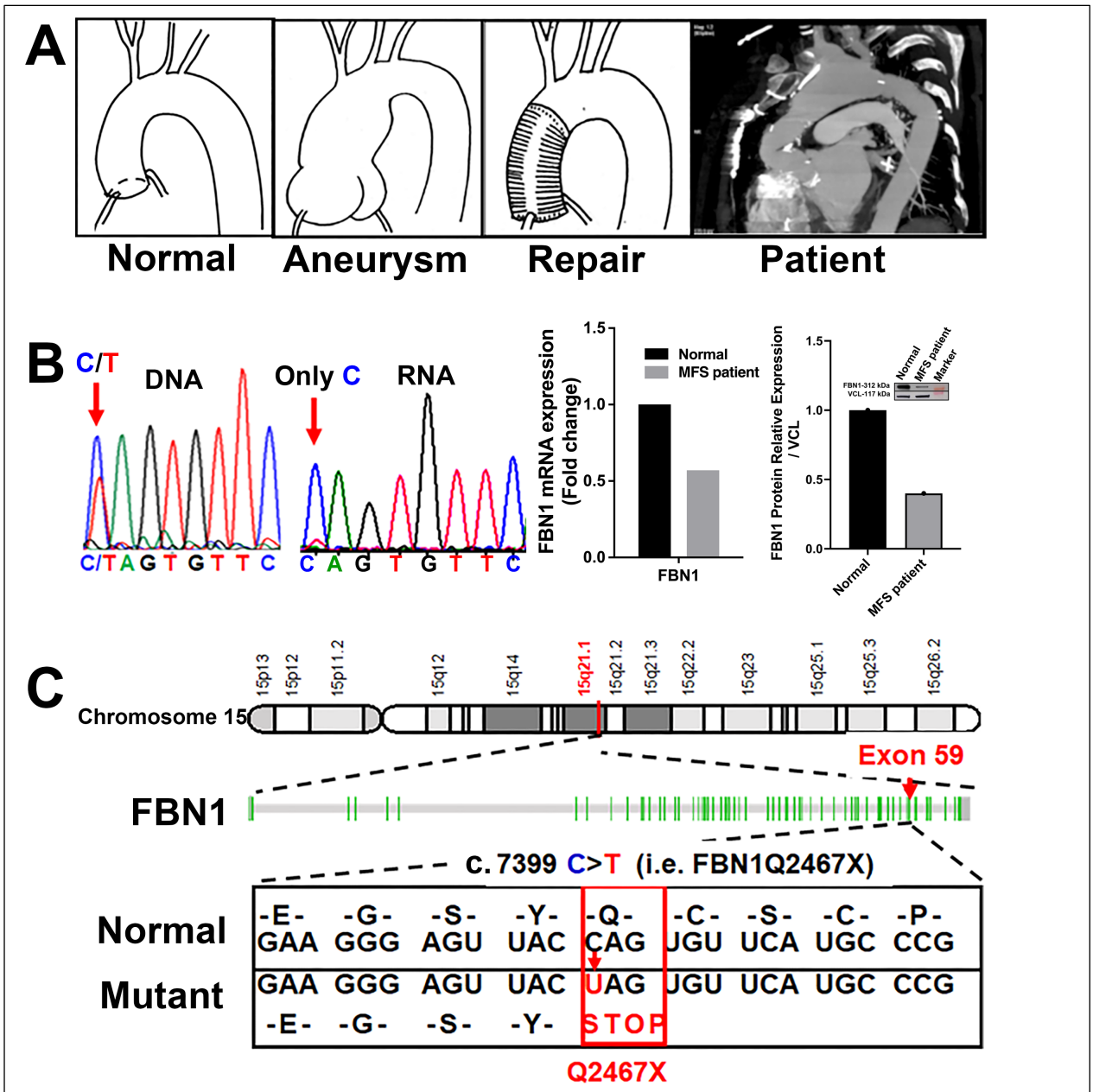

Figure 1. The *FBN1Q2467X* nonsense mutation associated with Marfan syndrome. (A) CT scan of a Marfan syndrome patient carrying the *FBN1Q2467X* mutation shows aneurysms in the thoracic aortic arch and evidence of prior surgical repair of the aortic root and ascending aorta.(B) Sanger sequencing chromatograms from the patient show both C and T peaks at position c.7399 in genomic DNA, whereas only the C allele is detected in cDNA, indicating degradation of transcripts carrying the mutant T allele. qPCR and Western blot analysis demonstrate ~50% reduced expression of *FBN1* mRNA and protein in the patient compared with a non-Marfan control. (C) Schematic representation of *FBN1* on chromosome 15, which spans 66 exons. The c.7399C>T transition in exon 59 introduces a premature stop codon (UAG), resulting in a nonsense mutation (Q2467X).

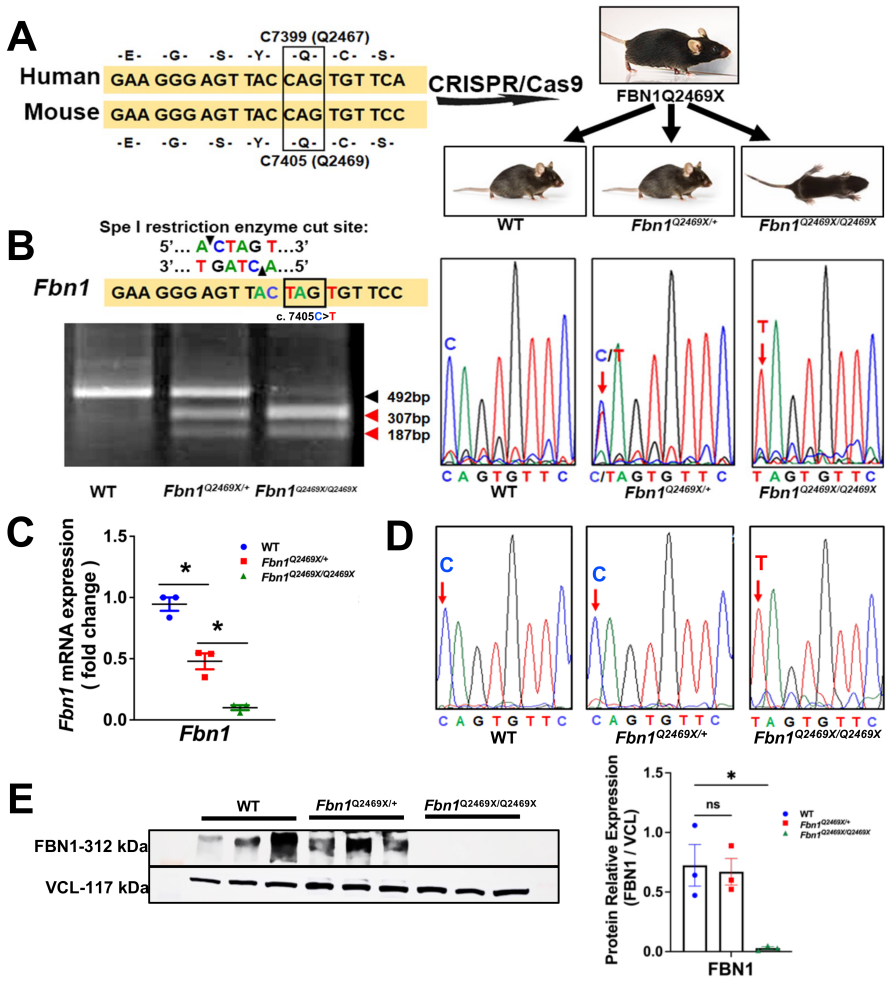

Figure 2. Generation and validation of the FBN1Q2469X Marfan mouse model. (A) Conservation of FBN1 between human and mouse. The human *c.7399C>T* mutation (Q2467X) in exon 59 corresponds to mouse *c.7405C>T* (Q2469X) in exon 60. CRISPR/Cas9 genome editing was used to introduce the *c.7405C>T* nonsense mutation into the mouse *Fbn1* gene, generating FBN1Q2469X mice. Breeding produced wild-type ($Fbn1^{+/+}$), heterozygous ($Fbn1^{Q2469X/+}$) and homozygous ($Fbn1^{Q2469X/Q2469X}$) genotypes. Representative pups at 10 days of age are shown. (B) Genotyping strategy. PCR products encompassing the mutation site were digested with SpeI, which is reconstituted only in the mutant allele (ACTAGT). The wild-type allele yields a single 492 bp band, while the mutant allele produces 307 bp and 187 bp fragments. Sanger sequencing chromatograms confirm the presence of the *c.7405C>T* mutation in heterozygous and homozygous mice. (C) *Fbn1* mRNA expression. qPCR shows a ~50% reduction of *Fbn1* mRNA in heterozygotes and >90% reduction in homozygotes (n=3; one-way ANOVA, $P<0.05$). (D) cDNA sequence analysis. Agarose gel electrophoresis of RT-PCR products (left) and corresponding Sanger chromatograms (right) demonstrate selective loss of the mutant transcript in heterozygotes, consistent with nonsense-mediated decay, while the mutant allele is retained in homozygotes. (E) FBN1 protein expression. Western blotting shows slightly reduced fibrillin-1 protein in heterozygotes and near-complete loss in homozygotes, relative to wild type. Vinculin (VCL) was used as a loading control (n=3; $P<0.05$).

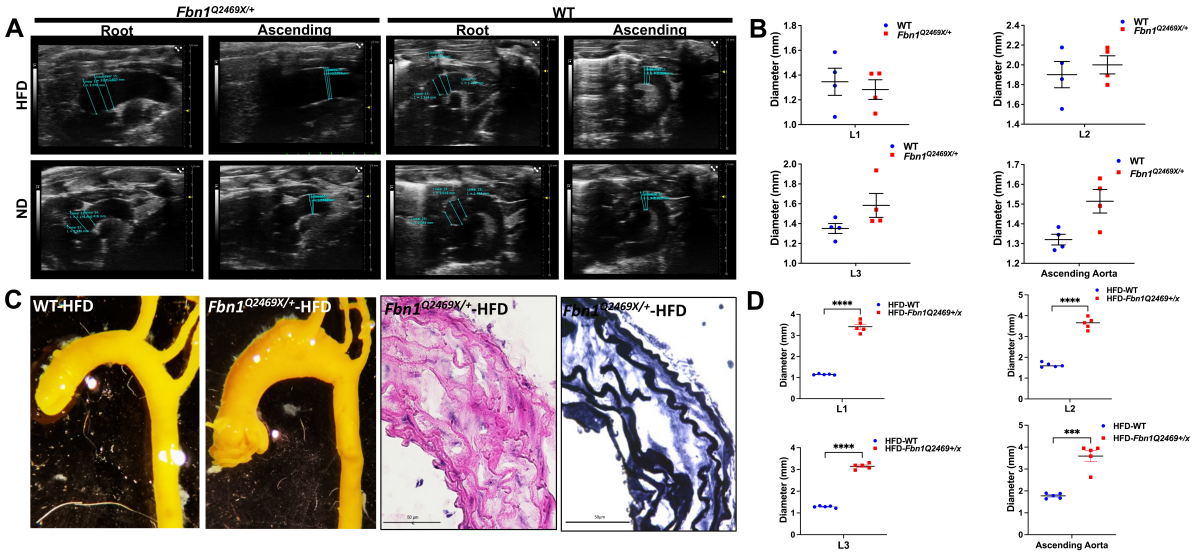

Figure 3. The Fbn1Q2469X/+ mice appear normal with slightly increased ascending aorta and decreases in blood pressure. But HFD induces significant dilation at the aortic root and ascending aorta. (A) Echocardiogram images show the diameters of the aortic annulus [L1], sinus of Valsalva [L2] and sino tubular junction [L3] in Fbn1Q2469X/+MFS mice (right side) versus the WT control mice (left side). (B)There is no significant dilation at the L1 and L2 of the aortic root; there are about 0.2mm dilation at L3 and 0.3mm dilation the ascending aorta, but there are no statistic difference (n=4). (C) Lax injection shows that High-fat diet induced aortic dilation in ascending aorta in *Fbn1*$^{Q2469X/+}$ mice. H&E and elastic fiber staining show significant VSMC dis organization and elastin fragmentation. (D) **H**FD treatment induced significant aortic dilation at L1, L2, L3 and ascending aorta (n=5).

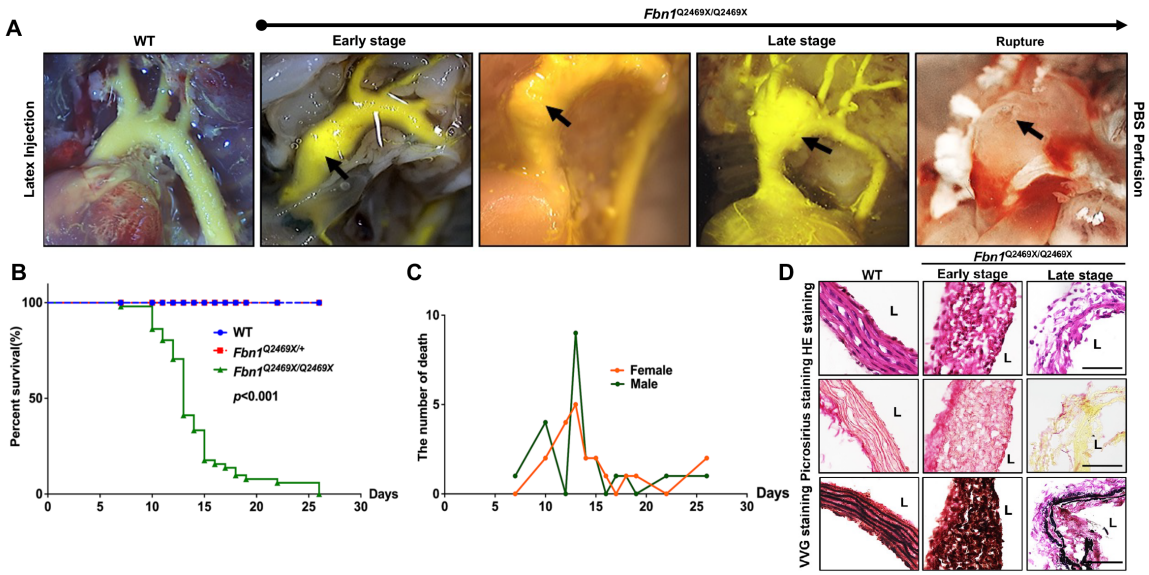

Figure 4. *Fbn1*$^{Q2469X/Q2469X}$ mice develop consistent progressive aneurysm, leading to rupture (A) *Fbn1*$^{Q2469X/Q2469X}$ mice show rapid aorta dilation during aneurysm progression from early stage, late stage to rupture. The images demonstrate the aneurysm progression and rupture in aortic root, ascending aorta and arch by the perfusion with PBS and followed by latex injection. Black arrows indicate the location of aneurysm dilation and rupture. (**B**) The Kaplan-Meier survival curve of mice for wild type (n=51), *Fbn1*$^{Q2469X/+}$ (n=70) and *Fbn1*$^{Q2469X/Q2469X}$ (n=51) mice. *P*<0.001. (**C**) There is no difference between male and female *Fbn1*$^{Q2469X/Q2469X}$ mice (n=20 for female; n=22 for male). (D) The pathological changes of aneurysm at ascending aorta during aneurysm progression from early stage to late stage. The H&E staining shows changes of the thickness, SMC organization in the vessel wall during aneurysm progression (Top). Picro sirius red staining shows collagen degradation in the aorta at late stage (middle). Verhoeff Van Gieson staining shows elastin disorganization at early stage and fragmentation at late stage.

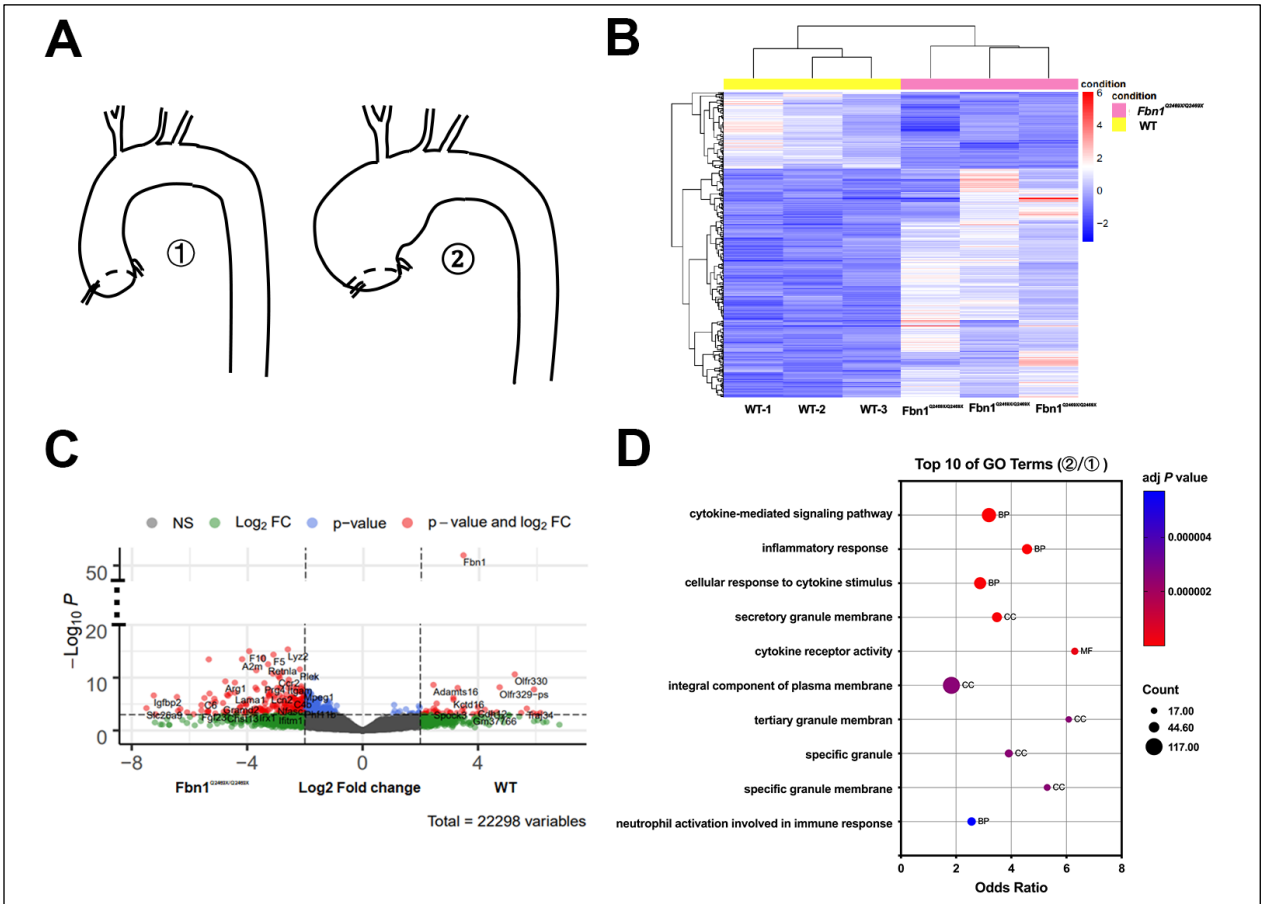

Figure 5. RNA-seq analyses reveal altered gene expression profiles in *Fbn1*$^{Q2469X/Q2469X}$ aneurysmal aortas. (A) Thoracic aortas from wild-type (WT) and *Fbn1*$^{Q2469X/Q2469X}$ mice (n=3 per group) were collected for RNA extraction and RNA-seq analysis. (B) Heatmap of the most variable genes (adjusted P<0.01), generated from variance-stabilized counts. The color scale reflects z-scores from the mean. Pearson correlation between samples was calculated using variance-stabilized counts, and sample distance was visualized as sqrt(1–cor²). (C) Volcano plot showing differentially expressed genes between WT and *Fbn1*$^{Q2469X/Q2469X}$ mice. The y-axis represents –log10 P values (P<0.01), and the x-axis represents log2 fold change. (D) Top 20 Gene Ontology (GO) terms enriched among differentially expressed genes, identified using DAVID. Red bars represent Biological Process terms, and the green bar represents a Molecular Function term.

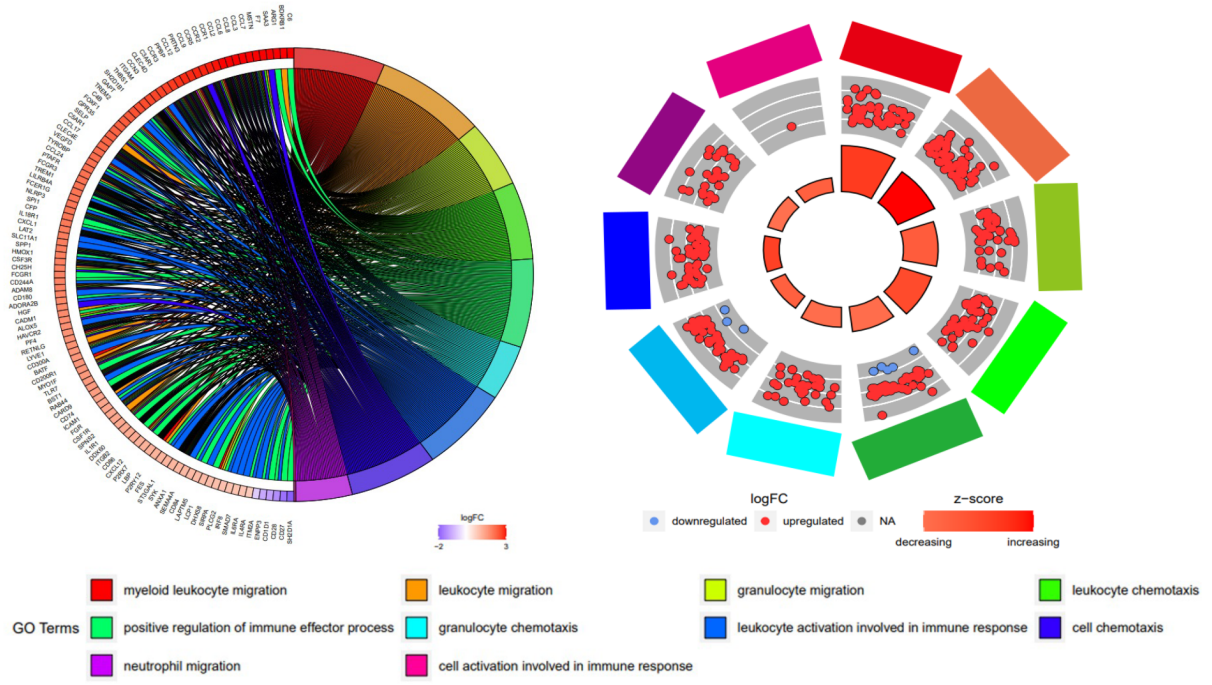

Figure 6. Gene Ontology enrichment analysis highlights inflammatory pathways in *Fbn1*$^{Q2469X/Q2469X}$ aneurysmal aortas. (A) Chord diagram showing the top 10 enriched GO terms and associated significantly differentially expressed genes between *Fbn1*$^{Q2469X/Q2469X}$ and WT aortas. Genes are color-coded by log2 fold change, with red indicating upregulation and purple indicating downregulation. GO terms are color-coded as indicated at the bottom. (B) Circular plot illustrating the top 10 inflammation-related GO terms. The outer ring represents individual GO terms, with upregulated genes in red and downregulated genes in blue. The inner circle is scaled by *P* value (larger size = greater significance) and color-coded by z-score, where red indicates pathway activation and blue indicates pathway suppression.

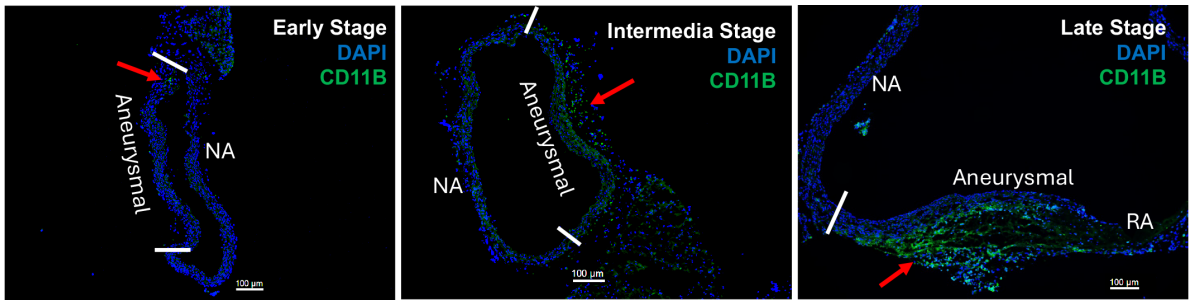

Figure 7. Progressive adventitial inflammation during aneurysm development. Immunofluorescence staining for CD11B demonstrates increasing immune cell infiltration in the adventitia of the aneurysmal vessel wall from early to late stages. At the early stage, few $CD11B^+$ cells are detected in the aneurysmal wall. At the intermediate stage, $CD11B^+$ cells are localized primarily to the adventitia of the aneurysmal region. At the late stage, $CD11B^+$ signals are markedly increased in the adventitia aneurysmal area near the rupture area. NA, nonaneurysmal area; RA, rupture area.

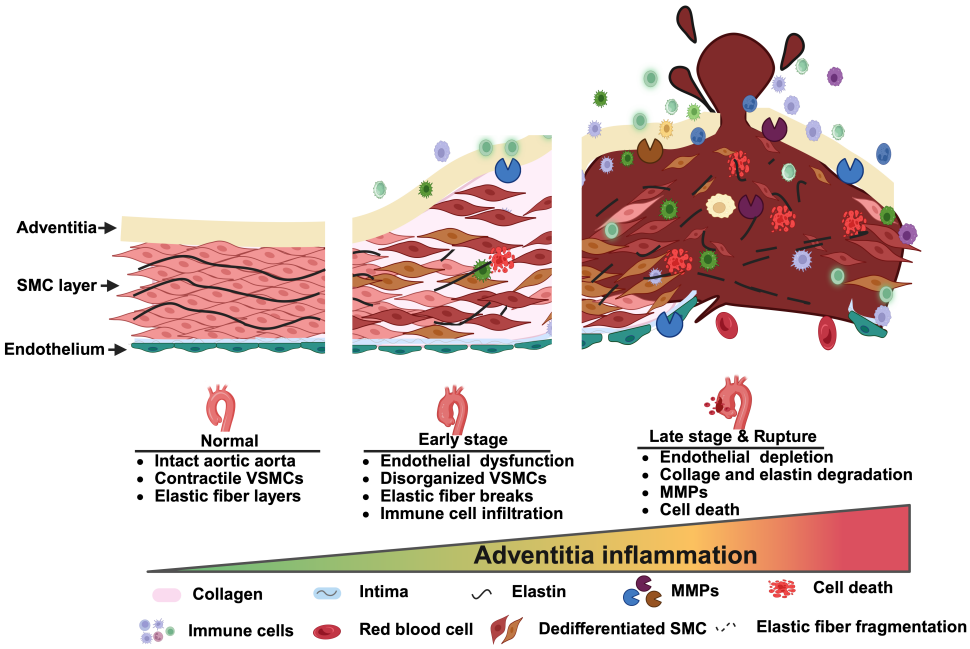

Figure 8. Summary of aneurysm progression and adventitial inflammation in FBN1Q2469X mouse model. Schematic model illustrating the structural and molecular changes during aneurysm progression from normal aorta to rupture. In the normal vessel, the aortic wall consists of intact endothelium, organized smooth muscle cells (SMCs), and elastic fibers. At early stage, aortic dilation is accompanied by SMC disorganization, elastic fiber breaks, and initial immune cell infiltration. In late-stage aneurysm and rupture, the vessel wall exhibits marked adventitial inflammation, collagen and elastic fiber degradation, matrix metalloproteinase (MMP) activation, cell death, and endothelial depletion. The gradient highlights the progressive increase of adventitial inflammation as a central driver of aneurysm progression to rupture. Symbols denote histological and molecular features, including collagen, elastin, intima, MMPs, immune cells, dedifferentiated SMCs, and elastic fragmentation.

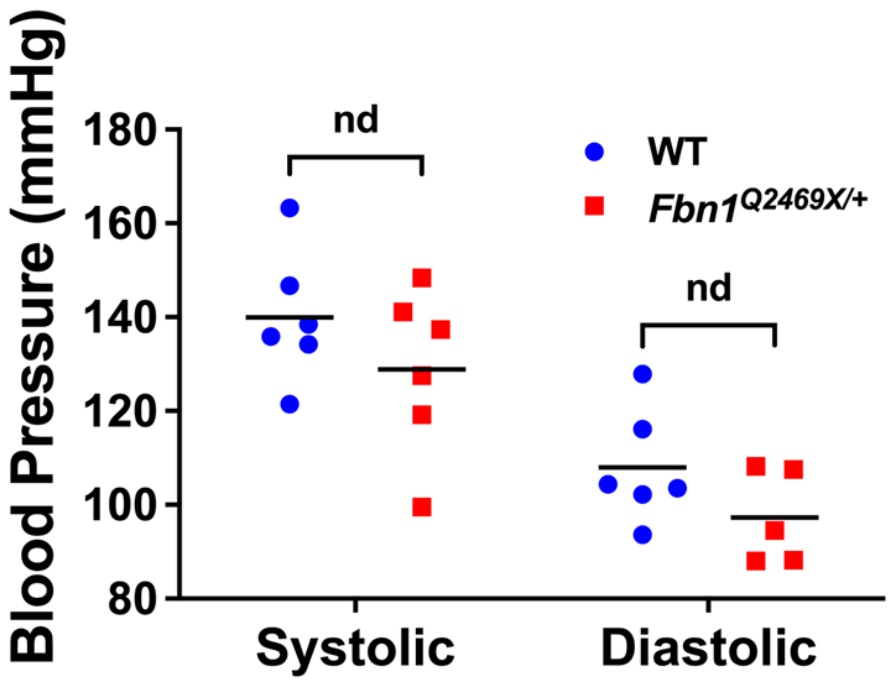

Figure S1. The blood pressure analyses in WT and *FBN1*$^{Q2469X/+}$ mice. There are no statistic difference between WT and *FBN1*$^{Q2469X/+}$ mice although the *FBN1*$^{Q2469X/+}$ mice show slightly decrease in blood pressure. n=10 both male and female mice are used.

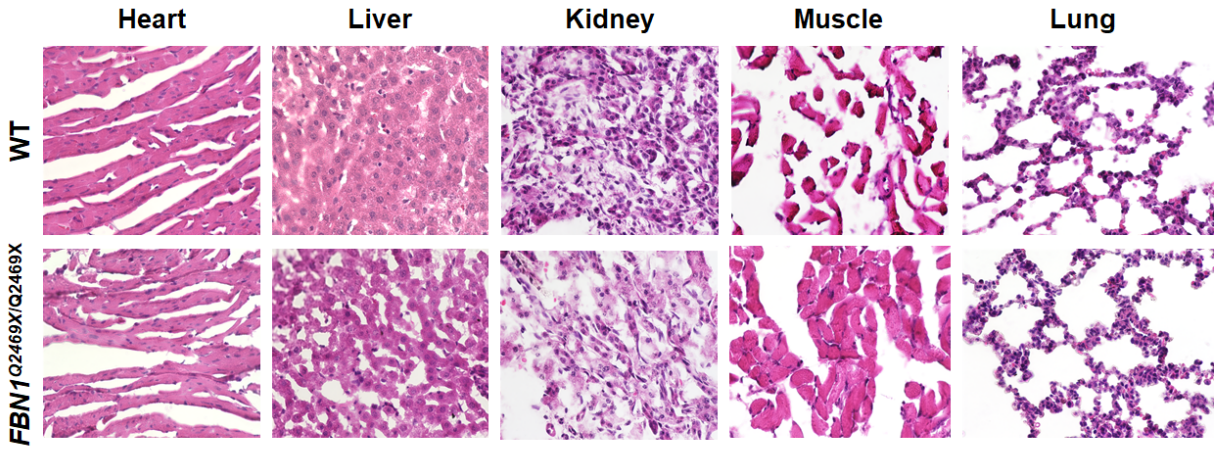

Figure S2. Histopathological analysis of systemic organs in WT and *Fbn1*$^{Q2469X/Q2469X}$ mice. Representative hematoxylin and eosin (H&E) staining of heart, liver, kidney, skeletal muscle, and lung tissues from wild-type (WT) and homozygous *Fbn1*$^{Q2469X/Q2469X}$ mice. Images were acquired at identical magnification to allow direct comparison. No major pathological abnormalities were observed in these organs, likely reflecting the young age of the pups at day 13.

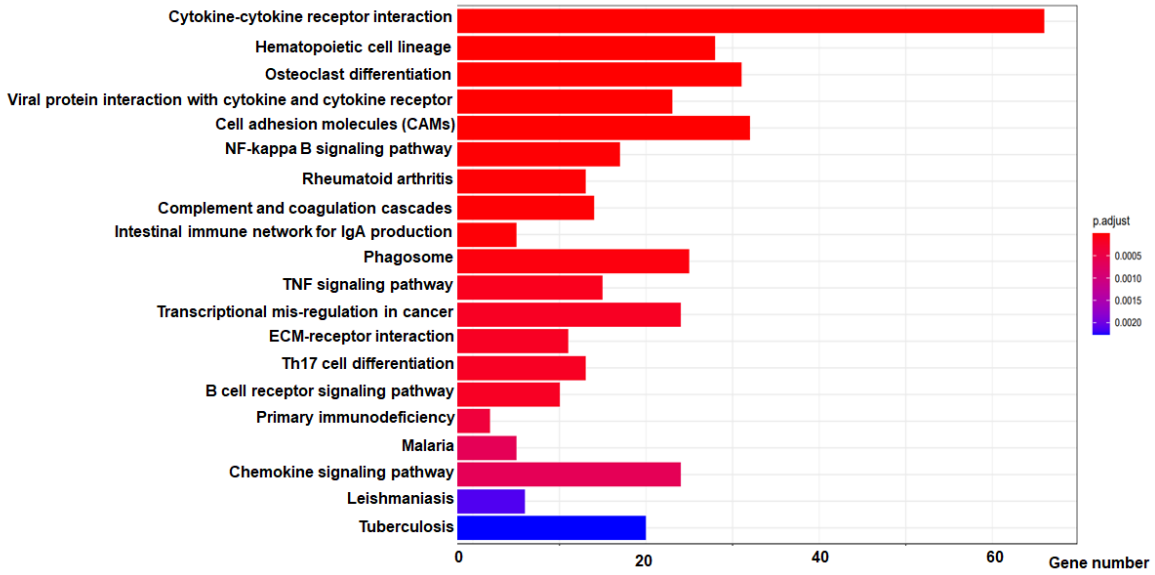

Figure S3. The KEGG analysis of RNA-seq data. The KEGG pathway enrichment analysis was generated with the significantly differentially expressed genes (P<0.01) in the RNA-seq of FBN1Q2469X/Q2469X mice and WT. Top 20 KEGG pathways are shown with bar plot: the color represent the adjusted p value of enrichment the KEGG pathways; X axis represents the gene number involved in the KEGG pathways.

Table S1 FBN1 **is highly conserved between human and mouse**

FBN1	**Human**	**Mouse**
Chromosome	**15**	**2**
Gene size	**237.4kb, 66 exons**	**66exons**
Exons/ATG/TAA	**66/2/66**	**66/2/66**
c.7399C>T transition	**In Exon 59 (CAG-TAG)**	**In Exon 60 (CAG-TAG)**
mRNA (NCBI)	**11756bp**	**9847bp**
Protein	**2873aa (350KD)**	**2873aa**
Protein identity	**2765/2873= 96.24%**	
Protein similarity	**2834/2873= 98.64%**	
a nonsense mutation	**Q2467X**	**Q2469X**